Driving the formation of the RbCs dimer by a laser pulse: A nonlinear-dynamics approach

C. Chandre,[1] Jorge Mahecha,[2] and J. Pablo Salas[3]

[1]*Aix Marseille Univ, CNRS, Centrale Marseille, I2M, Marseille, France*
[2]*Instituto de Física, Universidad de Antioquia (UdeA), Calle 70 No. 52-21, Medellín, Colombia*
[3]*Área de Física, Universidad de la Rioja, 26006 Logroño, La Rioja, Spain*

We study the formation of the RbCs molecule by an intense laser pulse using nonlinear dynamics. Under the Born-Oppenheimer approximation, the system is modeled by a two-degree-of-freedom rovibrational Hamiltonian, which includes the ground electronic potential energy curve of the diatomic molecule and the interaction of the molecular polarizability with the electric field of the laser. As the laser intensity increases, we observe that the formation probability first increases and then decreases after reaching a maximum. We show that the analysis can be simplified to the investigation of the long-range interaction between the two atoms. We conclude that the formation is due to a very small change in the radial momentum of the dimer induced by the laser pulse. From this observation, we build a reduced one-dimensional model which allows us to derive an approximate expression of the formation probability as a function of the laser intensity.

I. INTRODUCTION

During the past two decades, the development of sophisticated experimental techniques allowed one to use ultracold atoms to create two new states of matter that can be manipulated with high precision: the Bose-Einstein condensates (BECs) [1–3] and the degenerate Fermi gases (DFGs) [4–6]. Using the deep experimental background obtained with the investigations on BEC and on DFG, efforts have been dedicated to achieving a similar degree of control in molecular gases. Indeed, the production and manipulation of dense gases of cold and ultracold molecules constitute nowadays an active research field in atomic and molecular physics. In particular, starting from a gas of ultracold atoms, the photoassociation [7,8], the magnetoassociation [9], and the stimulated Raman adiabatic passage (STIRAP) [10] are among the usual techniques to create cold and ultracold molecules. These experimental techniques have been successfully applied to form different homonuclear and heteronuclear alkali-metal diatomic molecules in the rovibrational ground state, such as C_2 [11,12], LiCs [13], KRb [14], or RbCs [15–17]. Furthermore, a number of theoretical studies have guided and promoted many of the experimental achievements. Among other theoretical studies, we refer the reader to Refs. [18–20] and references therein. For a review about science, technology, and applications of cold and ultracold molecules, we refer to Ref. [21].

All the aforementioned techniques to create molecular bound states are based on the external control of the interactions of atoms and molecules with electromagnetic fields. From a classical point of view, it is of particular interest to study how the mechanical forces exerted by light on atoms and molecules perturb their motion. Moreover, the nonlinear nature of these forces make these systems very appealing for classical studies because, by the external control of the strengths of the interactions, we have at hand the possibility of tuning the system through different classical regimes. It is worth noting at this point that the use of classical mechanics to study microscopic systems is not new: Over the past three decades, a plethora of studies related to the classical

dynamics of atoms and molecules in external fields can be found in the literature. Some examples of such as studies can be found in Refs. [22–32]. Furthermore, classical studies in microscopic systems have revealed themselves as a power tool to understand quantum mechanical results in many cases (see, e.g., Refs. [22,32–36] and references therein).

Here we use nonlinear dynamics to explore the feasibility of creating cold diatomic molecules by using a strong linearly polarized laser pulse. While the usual techniques to create cold and ultracold diatomic molecules require the use of several excited electronic states, we describe here how the nonlinear mechanical force exerted by a laser field on an initially unbounded pair of cold atoms in their ground electronic state can lead to the formation of a bounded dimer. More precisely, we focus on the influence of the laser field in the formation of RbCs molecules. Besides the kinetic terms, the rovibrational Hamiltonian of the system includes two fundamental terms: namely, the potential energy curve between the Rb and Cs atoms and the interaction between the molecular polarizability and the laser field. Because the laser pulse contains an envelope with ramp-up, plateau, and ramp-down, the system depends explicitly on time and the corresponding Hamiltonian has $3 + 1/2$ degrees of freedom. However, by using spherical coordinates, the number of degrees of freedom can be reduced to $2 + 1/2$. For a convenient ensemble of initial conditions, we compute the formation probability as a function of the laser field strength for different values of the parameters of the pulse. In all cases we find that, as the field strength increases from zero, the formation probability first increases before reaching a maximum and then decreases for larger values of the field strength. It is worth noting that a similar behavior has been found in the ionization probability of atoms in the presence of an intense laser field [37,38]. From a detailed exploration of the dynamics of the system after the ramp-up, plateau, and ramp-down sequences of the laser pulse, we infer that the study of the formation mechanism can be reduced to the investigation of the long-range interaction between the two atoms. Indeed, we show that the formation is due to a very small change in the radial momentum of the dimer induced by the laser pulse. These observations

allow us to build a simplified one-dimensional Hamiltonian where only the long-range terms of the potential energy curve and the molecular polarizabilities are taken into account. From this simplified Hamiltonian, we obtain an analytic approximate expression for the formation probability as a function of the laser intensity. This analytic expression mimics very accurately the described behavior of the formation probability.

The paper is organized as follows: In Sec. II we present the main ingredients of the Hamiltonian of the system. In Sec. III we compute the formation probability as a function of the laser field strength. In order to get some insights into the behavior of the formation probability, we study the particular role played by the ramp-up, the plateau, and the ramp-down of the laser pulse. The results of Sec. III allow us to define in Sec. IV a one-dimensional version of the full Hamiltonian which captures the main characteristics of the system. In Sec. V we define the simplified Hamiltonian with only the long-range terms of the potential energy curve and the molecular polarizabilities. We show that this asymptotic Hamiltonian is sufficient to describe the behavior of the formation probability. Furthermore, we construct an analytic expression for the formation probability which includes the parameters of the laser pulse and the long-range parameters of the potential energy curve and the molecular polarizabilities.

II. THE HAMILTONIAN OF THE SYSTEM

Within the Born-Oppenheimer approximation, we describe the dynamics of the RbCs molecule in its $^1\Sigma^+$ electronic ground state in the presence of a strong linearly polarized laser field. The electric field of the laser is assumed to propagate in the parallel direction of the z axis of an inertial reference frame with the origin at the center of mass of the nuclei. For a

TABLE I. Values of the fitting parameter for the long-range behavior of the potential energy curve $\varepsilon(R)$ and the parallel and perpendicular polarizabilities $\alpha_{\parallel,\perp}(R)$. All parameters are given in atomic units.

$b_6 = 5284$	$b_8 = 730520$	$b_{10} = 1.0831 \times 10^8$
$c_2 = 1888.9$	$c_3 = -351865.9$	$c_4 = 1.5056 \times 10^6$
$d_2 = 1277.8$	$d_3 = 374596.4$	$d_4 = 2.7868 \times 10^6$

nonresonant laser field, the Hamiltonian of the system can be expressed as [39]

$$\mathcal{H} = \frac{P_R^2}{2\mu} + \frac{P_\theta^2}{2\mu R^2} + \frac{P_\phi^2}{2\mu R^2 \sin^2\theta} + V(R,\theta,t), \quad (1)$$

where μ is the reduced mass of the nuclei, (R,θ,ϕ) are the internuclear distance and the Euler angles, and (P_R, P_θ, P_ϕ) are the corresponding canonically conjugate momenta. $V(R,\theta,t)$ is the potential energy surface given by

$$V(R,\theta,t) = \varepsilon(R) + V_L(R,\theta,t), \quad (2)$$

which is made of the field-free adiabatic electronic potential energy curve $\varepsilon(R)$ and the laser-molecule interaction potential $V_L(R,\theta,t)$,

$$V_L(R,\theta,t) = -g(t)\frac{F^2}{4}[\alpha_{\parallel}(R)\cos^2\theta + \alpha_{\perp}(R)\sin^2\theta]. \quad (3)$$

The function $g(t)$ is the laser pulse envelope and F is the strength of the electric field of the laser. The functions $\alpha_{\parallel,\perp}(R)$ are the parallel and the perpendicular molecular polarizabilities [40]. The pulse envelope $g(t)$ contains a ramp-up, a plateau, and a ramp-down with durations T_{ru}, T_p, and T_{rd}, respectively, and its profile is taken to be [41]

$$g(t) = \begin{cases} \sin^2\left(\frac{\pi t}{2T_{ru}}\right) & \text{if } 0 \leqslant t < T_{ru}, \\ 1 & \text{if } T_{ru} \leqslant t < T_{ru} + T_p, \\ \sin^2\left(\frac{\pi(t - T_{ru} - T_p - T_{rd})}{2T_{rd}}\right) & \text{if } T_{ru} + T_p \leqslant t < T_{ru} + T_p + T_{rd}, \\ 0 & \text{elsewhere.} \end{cases} \quad (4)$$

This field envelope describes accurately experimental laser pulses [42].

In order to manage an analytical representation for the potential energy surface $V(R,\theta,t)$ for the RbCs molecule, we have fitted the available data of $\varepsilon(R)$ [43] and $\alpha_{\parallel,\perp}(R)$ [40] to three appropriate functional forms. In the case of $\varepsilon(R)$, the fitting function of the *ab initio* data includes the long-range behavior of the energy curve, which is expressed as [44]

$$\varepsilon_{LR}(R) = -\frac{b_6}{R^6} - \frac{b_8}{R^8} - \frac{b_{10}}{R^{10}}. \quad (5)$$

For the $^1\Sigma^+$ RbCs these coefficients can be found in the literature [44] and their values are reported in Table I. The asymptotic behavior of the polarizabilities $\alpha_{\parallel,\perp}(R)$ is well described by the Silberstein

expressions [45,46]

$$\alpha_{\parallel}^{LR}(R) = \frac{\alpha_{RbCs} + 4\alpha_{Rb}\alpha_{Cs}/R^3}{1 - 4\alpha_{Rb}\alpha_{Cs}/R^6},$$

$$\alpha_{\perp}^{LR}(R) = \frac{\alpha_{RbCs} - 2\alpha_{Rb}\alpha_{Cs}/R^3}{1 - \alpha_{Rb}\alpha_{Cs}/R^6}, \quad (6)$$

where $\alpha_{Rb} \approx 313$ a.u. and $\alpha_{Cs} \approx 394$ a.u. are the atomic polarizabilities of the atoms and $\alpha_{RbCs} = \alpha_{Rb} + \alpha_{Cs}$. The two Silberstein expressions (6) diverge when $R \to (4\alpha_{Rb}\alpha_{Cs})^{1/6} \approx 8.8889$ a.u. and $R \to (\alpha_{Rb}\alpha_{Cs})^{1/6} \approx 7.0552$ a.u., respectively. This is a drawback for classical calculations. Taking into account that computational data for the molecular polarizabilities are available up to the intermolecular distance of $R = 30$ a.u., instead of using the analytical expression (6) to model the long-range behavior of $\alpha_{\parallel,\perp}$, we append to the computational
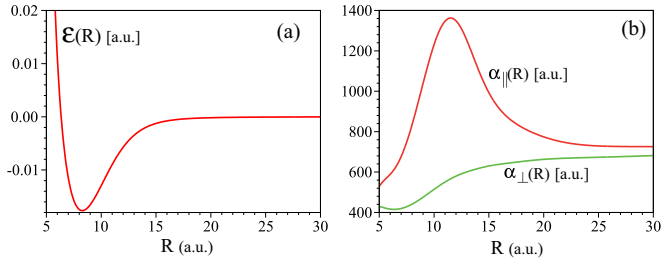
FIG. 1. (a) Electronic potential energy curve $\varepsilon(R)$ of the RbCs and (b) parallel $\alpha_\parallel(R)$ and perpendicular $\alpha_\perp(R)$ components of the molecular polarizability of the RbCs molecule.

data of the molecular polarizabilities, values of $\alpha_{\parallel,\perp}$ evaluated for $R > 30$ a.u. at the Silberstein expressions (6). This allows us to fit the polarizabilities $\alpha_{\parallel,\perp}$ with smooth functions which are very convenient for classical calculations. The long-range fittings for $\alpha_{\parallel,\perp}(R)$ are given by

$$\alpha_\perp^{LR}(R) = \alpha_{RbCs} + \frac{c_2}{R^2} + \frac{c_3}{R^3} + \frac{c_4}{R^4}, \qquad (7)$$

$$\alpha_\parallel^{LR}(R) = \alpha_{RbCs} + \frac{d_2}{R^2} + \frac{d_3}{R^3} + \frac{d_4}{R^4}. \qquad (8)$$

The fitting parameters b_i, c_i, and d_i are shown in Table I. The fitted curves $\varepsilon(R)$ and $\alpha_{\parallel,\perp}(R)$ are plotted in Fig. 1.

Owing to the continuous axial symmetry of the system, the polar angle ϕ is cyclic in Hamiltonian (1) and the z component P_ϕ of the angular momentum is conserved. This allows one to consider the expression (1) as a classical Hamiltonian system with $2 + 1/2$ degrees of freedom in (R,θ). The $1/2$ degree of freedom is due to the explicit time dependence in $\mathcal{H}$. The present study is restricted to the $P_\phi = 0$ case, i.e., the corresponding magnetic quantum number is zero, being this particular value widely used is several studies [47,48]. The landscape of the potential energy surface $V(R,\theta,t)$ during the plateau $[g(t) = 1]$ is strongly determined by the polarizability. Indeed, as we can observe in Fig. 2, for $F = 1.5 \times 10^{-3}$ a.u., the energy surface $V(R,\theta,t)$ presents four critical points: two equivalent minima $P_{1,2}$ at $\theta = 0,\pi$ respectively, a saddle point P_3 at $\theta = \pi/2$ and a maximum P_4 at $\theta = \pi/2$. These critical points create two different regions of motion. When the energy of the molecule is below the energy of the saddle point P_3, the rovibrational motion of the dimer is made of pendular states [49] around the minima $P_{1,2}$ because the molecule is confined in one of the potential wells around $P_{1,2}$. In other words, we find the expected behavior of a dimer aligned in the $\theta = 0,\pi$ directions [50]. On the other hand, when the energy of the system is above the saddle-point energy, the molecule can describe complete rotations. Due to the so-called energy hill around the maximum P_4 created by the polarizability, the molecular bond R always reaches its largest values along the $\theta = 0,\pi$ directions. As the electric field strength F increases, the maximum P_4 approaches the saddle point P_3 and its energy increases. The directions $\theta = 0,\pi$ together with the threshold dissociation conditions $R \to \infty$, $P_R \to 0$, and $P_\theta \to 0$ allow us to get an analytical estimate of the dissociation energy E_d. Under the condition $R \to \infty$, the function $\varepsilon(R)$ tends to 0, and $\alpha_\parallel(\infty) = \alpha_\perp(\infty) = \alpha_{Rb} + \alpha_{Cs}$. Then, the approximate
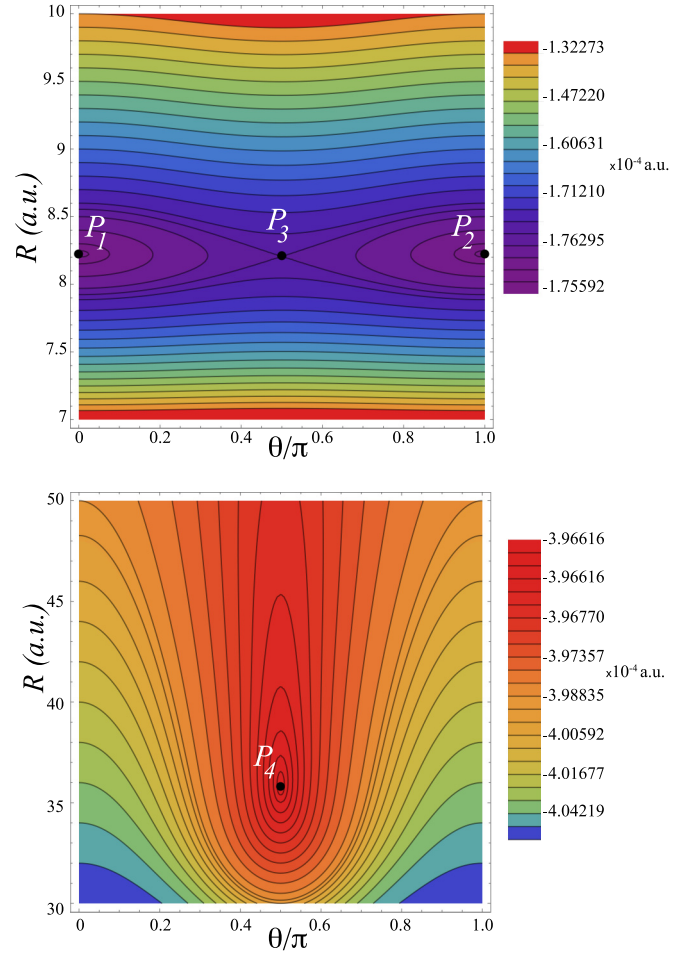

FIG. 2. Equipotential curves of the potential energy surface $V(R,\theta,t)$ during the plateau $[g(t) = 1]$ for a laser field strength $F = 1.5 \times 10^{-3}$ a.u.

value for the dissociation energy is given by

$$E_d \approx -\frac{F^2}{4}\,\alpha_\parallel(\infty) = -\frac{F^2}{4}\,(\alpha_{Rb} + \alpha_{Cs}). \qquad (9)$$

Thus, the molecular polarizabilities lead to a decrease of the dissociation energy to a negative value, which depends on the electric field strength F as well as on the polarizabilities of the atoms.

III. DRIVING THE FORMATION OF THE DIMER: NUMERICAL EXPERIMENTS

We use Hamiltonian (1) to study the impact of the laser field in the creation of bound molecular states. In particular, we compute numerically the formation probability $P(F)$ as a function of the field strength F. To do that, we consider a large ensemble of initially free pairs of Rb-Cs atoms, whose dynamics is governed by the free Hamiltonian

$$\mathcal{H}_0 = \frac{P_R^2}{2\mu} + \frac{P_\theta^2}{2\mu R^2} + \varepsilon(R). \qquad (10)$$

All the initial conditions $(R_0, P_R^0, \theta_0, P_\theta^0)$ of the ensemble have the same positive energy $\mathcal{H}_0 = E_0 = 3 \times 10^{-9}$ a.u. This
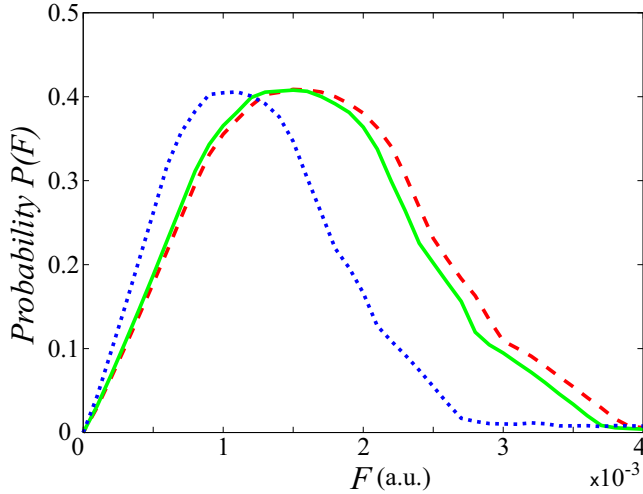
FIG. 3. Formation probability as a function of F for an initial energy $E_0 = 3 \times 10^{-9}$ computed from Hamiltonian (1). The parameters of the pulse are $T_{ru} = T_{rd} = 5$ ps and $T_p = 70$ ps (shaded red line), $T_{ru} = T_{rd} = 15$ ps and $T_p = 70$ ps (solid green line) and $T_{ru} = T_{rd} = 15$ ps and $T_p = 140$ ps (dotted blue line), respectively.
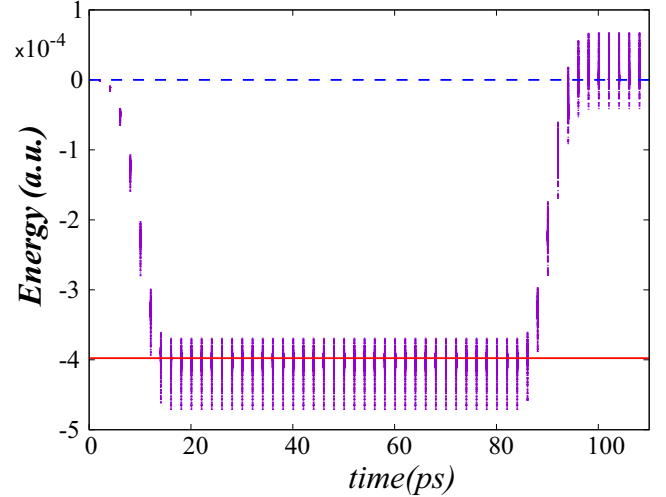

FIG. 4. Evolution of the energy of an ensemble of trajectories with initial energy $E_0 = 3 \times 10^{-9}$ a.u. The amplitude of the laser field is $F = 1.5 \times 10^{-3}$ a.u. The parameters of the pulse are $T_{ru} = T_{rd} = 15$ ps and $T_p = 70$ ps. The solid red and the dashed blue lines indicate the dissociation energy (9) and the zero energy, respectively.

energy roughly corresponds to the temperature $T = 1$ mK of a sample of cold atoms in a typical photoassociation experiment [7,51]. The choice of the initial states is an important issue as it is shown later on. Here P_θ^0 is taken to be zero, θ_0 is chosen randomly in $[0,\pi]$, and R_0 is chosen in the interval $[R_{min}, R_{max}] = [6.2319, 100]$ a.u., where R_{min} is the (inner) turning point of the phase trajectory of Hamiltonian (10) for $P_\theta^0 = 0$. First, let us compute the time evolution of the (unbound) trajectory of energy $E_0 = 3 \times 10^{-9}$ a.u. starting at the initial internuclear distance $R_0 = R_{max}$ and with the inward initial radial momentum $P_R^0 \approx -0.04$ a.u. given by Eq. (10). We consider this orbit until it reaches again R_{max} with $P_R \approx 0.04$ a.u. When the intermolecular distance $R(t)$ of this trajectory is mapped at equal time intervals, we observe that large values of $R(t)$ are rapidly reached. In other words, the initial conditions with large values of R_0 are more likely than initial conditions with small values of R_0. In this way, in order to mimic more accurately the initial states of the system, we choose the initial conditions (R_0, P_R^0) along the phase curve (10) for E_0 at equal time steps. It is worth noting that, with these initial conditions uniformly distributed over time, less than a 1% of the initial conditions have values of $R_0 < 25$ a.u.

By the numerical integration of the equations of motion arising from Hamiltonian (1), we propagate the ensemble of trajectories for the entire pulse duration. If after the pulse the energy of a given trajectory is negative, a bound state is then created. Otherwise, the trajectory remains unbounded. In our numerical experiments we consider laser pulses with electric field F amplitude between 0 and 4×10^{-3} a.u., which corresponds to a laser field of maximal intensity of 10^{12} W cm^{-2}. The $T_{ru} + T_p + T_{rd}$ total duration of the pulse is taken between 80 and 170 ns. In Fig. 3 the formation probability $P(F)$ as a function of the electric field strength F for three different laser profiles is represented. Since we start with a positive initial energy, the formation probability is

zero for $F = 0$. It then increases sharply with F up to a given critical value of F which depends of the pulse envelope $g(t)$, and then it decreases with F. Our objective is to analyze the reversal behavior observed in the formation curves in order to assess the role of the different parts of the pulse in the building up of this curve. To this end, we analyze separately the role of the ramp-up, the plateau, and the ramp-down in the dynamics of the system. Special attention is put on the study of the dynamics during the plateau because this study provides important information about the phase space structure of the system and its possible impact in the formation mechanism. Although results are not being reported here, it is worth noting that from the computations with ensembles of trajectories with initial conditions where P_ϕ and P_θ were not necessarily fixed to zero, the formation probability has exactly the same shape observed in Fig. 3. In this way, this reversal behavior seems to be very robust and not restricted to trajectories with initial conditions on the invariant manifold $P_\phi = 0$ and with initial conditions $P_\theta = 0$.

A. Role of the ramp-up of the laser pulse

In Fig. 4 the evolution as a function of time of the energy of a bunch of representative trajectories with initial energy E_0 is represented for an amplitude of the laser field of $F = 1.5 \times 10^{-3}$ a.u. The parameters of the pulse are $T_{ru} = T_{rd} = 15$ ps and $T_p = 70$ ns. As expected, the role of the ramp-up is to decrease the energy of the system and to promote the initially unbounded trajectories in a region where, potentially, they might be bounded. After the ramp-up, the energy probability is represented in Fig. 5 (dashed red line).

This energy distribution indicates that, after the ramp-up, a big amount of trajectories acquire energy values around a relatively narrow region. This peak structure is easily understood assuming that the dynamics does not play a major role. Under this assumption, the energy E_f at the end of the
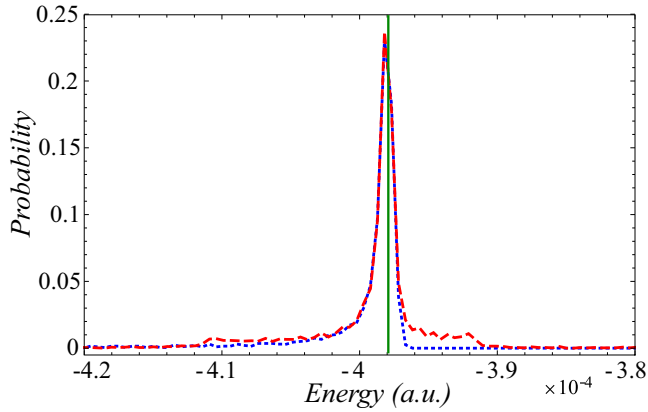
FIG. 5. Probability distribution of the energy of an ensemble of trajectories with an initial energy $E_0 = 3 \times 10^{-9}$ a.u. after a ramp-up of 15 ps (dashed red line). The dotted blue line is the probability energy distribution of an ensemble given by Eq. (11). The dissociation energy E_d for this electric field is denoted with the solid green vertical line. The parameters of the pulse are $T_{ru} = T_{rd} = 15$ ps and $T_p = 70$ ps and the amplitude of the electric laser field is $F = 1.5 \times 10^{-3}$ a.u.

ramp-up is approximately

$$E_f \approx \varepsilon(R) - \frac{F^2}{4}[\alpha_{\parallel}(R)\cos^2\theta + \alpha_{\perp}(R)\sin^2\theta], \quad (11)$$

In Fig. 5 the dashed blue line is the probability distribution given by E_f, where θ and R are evaluated in the ensemble of trajectories after the ramp-up. We notice that this distribution displays the same peak structure as the distribution of energies after the ramp-up computed from the equations of motion associated with Hamiltonian (1). The peak is located around the maximum of E_f for R_{max}, which is the maximum distance considered in the ensemble of initial conditions. This maximum of energy almost corresponds to the dissociation energy $E_d \approx 3.977 \times 10^{-4}$ a.u. for $F = 1.5 \times 10^{-3}$ a.u. This value is denoted with the green vertical line in Fig. 5. Around $R = R_{max}$, the potential $\varepsilon(R)$ is negligible. This means that most of the trajectories have energies as if they were at $R = R_{max}$. This comes from the fact that the potential is rather flat for $R \geqslant 30$, which affects more than 75% of the trajectories. Therefore, the dynamics is very slow for these trajectories, and θ and R are approximately constant over the duration of a ramp-up of a few picoseconds.

B. Dynamics during the plateau

During the plateau, Hamiltonian (1) is autonomous and with two degrees of freedom. We visualize the nonlinear dynamics using Poincaré surfaces of section. A convenient Poincaré section is $P_R = 0$ with $\dot{P}_R > 0$, represented in the plane (θ, P_θ). Since we would like to gain insight into the formation probability, we look at bounded trajectories for which the distance R is oscillating in time. In addition, to compute the surface of section we select the value of the most probable energy, i.e., the peak in Fig. 5 which roughly corresponds to $E = -3.98 \times 10^{-4}$ a.u. For a single value of (θ, P_θ) there are two possible values of R, one close to the inner turning point and another one for a larger value of R close the outer turning point. The first one corresponds to
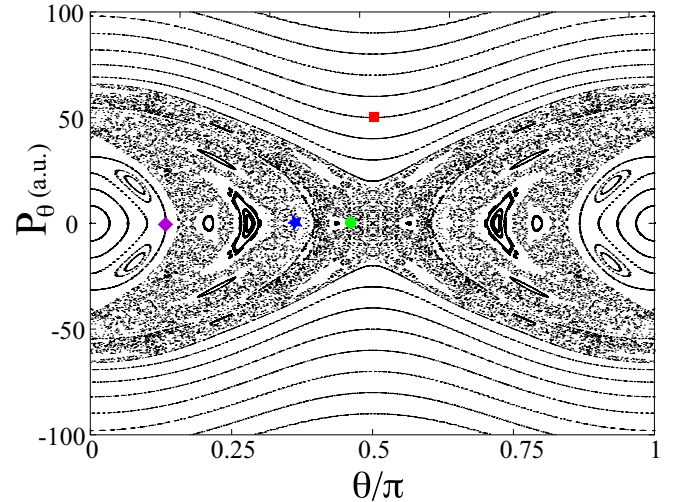

FIG. 6. Poincaré section ($P_R = 0$, $\dot{P}_R < 0$) of Hamiltonian (1) for an energy $E = -3.98 \times 10^{-4}$ a.u. and for an electric field $F = 1.5 \times 10^{-3}$ a.u.

$\dot{P}_R > 0$ and the second one to $\dot{P}_R < 0$. In order to draw the Poincaré section, we must allow the trajectory to cross the section a relatively high number of times, so we consider the long-term dynamics much larger than the duration of the laser pulse. A Poincaré section of Hamiltonian (1) is represented on Fig. 6. Each initial condition is integrated up to 10^5 ps.

We notice that for a reasonable range of values of P_θ the dynamics resembles the one of a forced pendulum with rotational and librational trajectories, and a rotational chaotic zone around the hyperbolic point at $\theta = \pi/2$ [30]. We use the term *rotational* chaotic zone to indicate the chaotic trajectories spanning the whole interval $[0,\pi]$ for the angle θ. We observe a different librational chaotic zone around the elliptic points (located at $\theta = 0$ and $\theta = \pi$), which is apparently disconnected from the rotational chaotic zone, at least on the duration of the numerical integration we have performed. The elliptic points at $\theta = 0, \pi$ correspond to two straight radial oscillations from R_a to R_b. These values R_a and R_b are the two solutions of $\varepsilon(R) - F^2\alpha_{\parallel}(R)/4 = E$. We refer to these radial periodic orbits as I_R. In Fig. 7 some sample trajectories are shown. The initial conditions of these orbits are taken on the surface of a section of Fig. 6. A rotational trajectory is depicted in Fig. 7(a); these trajectories live on two-dimensional invariant tori. The orbit in Fig. 7(b) is an example of chaotic trajectory in the rotational chaotic zone. We notice that the interatomic distances of these two trajectories do not reach large values. Figure 7(c) shows a trajectory in the librational chaotic zone; indeed, we notice that the trajectory does not span the whole interval of definition of the angle θ. Finally, in Fig. 7(d) a trajectory in a regular elliptic island near the elliptic fixed point around $\theta = 0$ is shown. We notice that these last two trajectories reach very large values of R. As expected, all trajectories remain bounded since the energy $E = -3.98 \times 10^{-4}$ a.u. is below the dissociation energy $E_d \approx 3.977 \times 10^{-4}$ for $F = 1.5 \times 10^{-3}$ a.u.

What is not apparent in the Poincaré section of Fig. 6 is the time scales of the dynamics. In order to illustrate this property, we plot the first recurrence time (the time it takes a trajectory
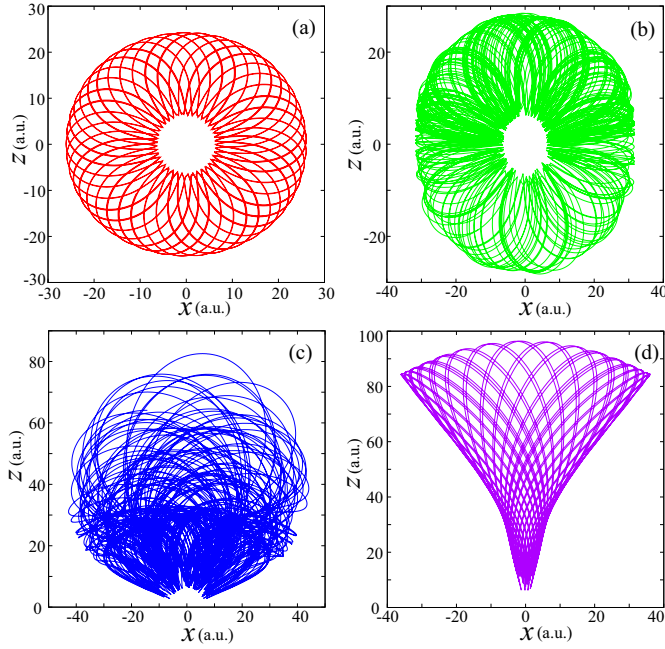
FIG. 7. Trajectories in the plane $(R \sin \theta, R \cos \theta)$ of Hamiltonian (1) for $F = 1.5 \times 10^{-3}$ a.u. and energy $E_0 = -3.98 \times 10^{-4}$ a.u. (a) Rotational trajectory with initial conditions $\theta = \pi/2$, $P_\theta = 50$, and $P_R = 0$ (red square in Fig. 6); (b) rotational chaotic trajectory with initial conditions $\theta = 1.45$, $P_\theta = 0$, and $P_R = 0$ (green dot in Fig. 6); (c) vibrational chaotic trajectory with initial conditions $\theta = 1.1$, $P_\theta = 0$, and $P_R = 0$ (blue star in Fig. 6); and (d) vibrational regular trajectory with initial conditions $\theta = 0.2$, $P_\theta = 0$, and $P_R = 0$ (purple diamond in Fig. 6).

to cross the Poincaré section for the first time after starting on the Poincaré section) as a function of (θ, P_θ) on the Poincaré section. The recurrence time map corresponding to the surface of section of Fig. 6 is shown in Fig. 8. As we can observe in this color map, in the rotational zones, the dynamics is rather fast (of the order of tens of ps), while in the librational zones
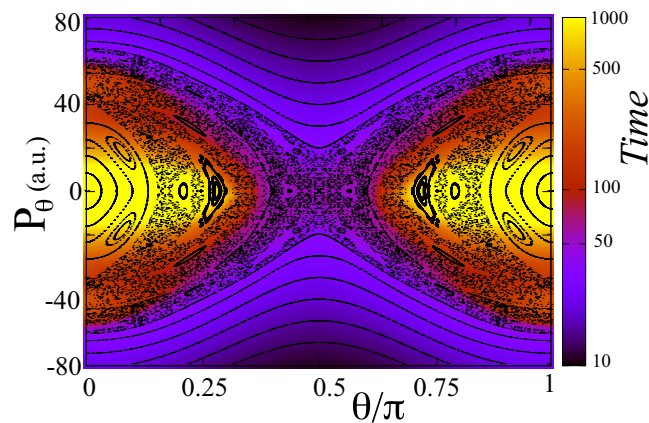

FIG. 8. First recurrence time (in ps) in the Poincaré section ($P_R = 0$, $\dot{P}_R < 0$) in the plane (θ, P_θ) for $F = 1.5 \times 10^{-3}$ a.u. and energy $E = -3.98 \times 10^{-4}$ a.u. The color axis has been saturated at 1000 ps for clarity. In the middle region, the recurrence time reaches above 1400 ps. Note that a logarithmic scale is used in the color code.
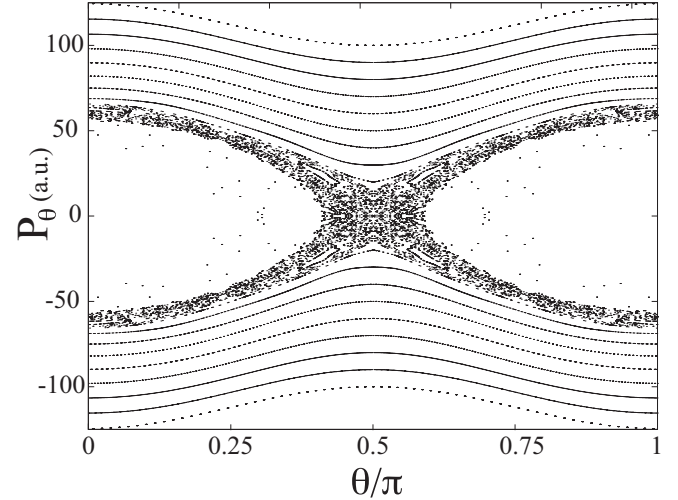

FIG. 9. Poincaré section ($P_R = 0$, $\dot{P}_R < 0$) of Hamiltonian (1) for an energy $E = -3.976 \times 10^{-4}$ a.u. and for an electric field $F = 1.5 \times 10^{-3}$ a.u.

the dynamics is much slower (on the order of a thousand ps). This is due to the fact that the trajectories in the librational zones [see Figs. 7(c) and 7(d)] reach rather large values of R where the potential is extremely flat and hence the dynamics is potentially extremely slow.

During the plateau of the pulse, for $E < E_d$ [see Eq. (9)], the trajectories are bounded and the ones which are the most stretched are around the radial modes I_R. As the energy E gets closer to E_d, the maximum radius R_b of I_R increases rapidly. When the energy crosses the value E_d, the radial trajectories I_R and the quasiperiodic orbits surrounding them are the first orbits to be unbounded because these orbits are localized along the dissociation channels at $\theta = 0, \pi$. This fact is observed in the Poincaré section of Fig. 9 where the holes in the regions around $\theta = 0, \pi$ correspond to the unbounded trajectories.

C. Dynamics during the ramp-down

As we observe in Fig. 4, the expected role of the ramp-down is to increase the energy of the trajectories. Note that not all the bounded dressed states, i.e., the bounded states in the presence of the laser field, remain bounded after the ramp-down. When the energy probability distribution after the ramp-down is calculated (see Fig. 10), we observe a strong peak structure which indicates that, after the ramp-down, most of the trajectories have energies in a narrow region around zero.

Where are the formed trajectories in phase space? This is a particularly difficult question to address since, besides the dependence of the formed trajectories with the initial conditions, it highly depends on the parameters of the laser pulse (like the intensity, the duration of the ramp-up, plateau, and ramp-down). In particular, it is not possible to predict on the Poincaré section represented in Fig. 6 which initial conditions lead to formation and which ones to dissociation. The main reason is that, depending on the duration of the pulse, the same initial condition can lead to formation or dissociation. One of the noticeable features is that the formed trajectories
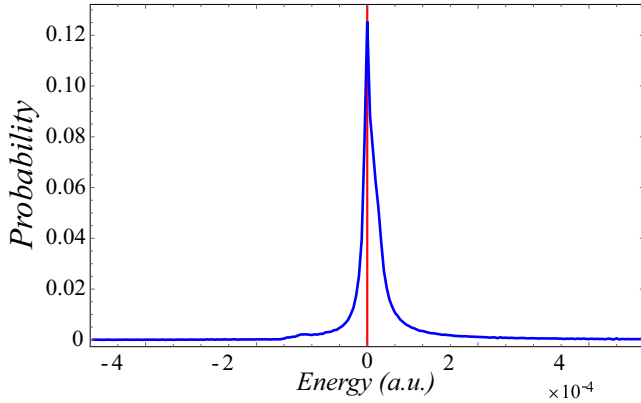
FIG. 10. Probability distribution of the energy of an ensemble of trajectories with an initial energy $E_0 = 3 \times 10^{-9}$ a.u. after the a ramp-down of 15 ps. The vertical red line indicates the zero energy value. The amplitude of the laser field is 1.5×10^{-3} a.u. and the parameters of the pulse are $T_{ru} = T_{rd} = 15$ ps and $T_p = 70$ ps.

have a finite range for the distance, meaning that if the distance between the two atoms is too large, it will not lead to formation. For instance, for $F = 1.5 \times 10^{-3}$, this maximum distance is about 130 a.u. In Fig. 11 we represent the histograms of initial distances leading to formation compared to the ones which lead to dissociation, where we notice that after some fixed initial distance, the formation is no longer possible. We also notice that the trajectories leading to formation are the ones with small values of P_θ, especially at the end of the laser pulse.

From the pendulum-like structure of the Poincaré map of Fig. 6, we know that the phase space is populated with two main types of trajectories, namely, vibrational and rotational trajectories. As we illustrate in Fig. 7, the vibrational orbits reach the largest interatomic distances. Thence, because the dimer must be formed with trajectories connecting large and small values of R and most of the orbits have initial conditions with values of $R_0 > 25$ a.u., we can argue that vibrational trajectories should play a dominant role in the formation mechanism. Moreover, because the radial mode I_R is the simplest vibrational orbit, it is expected to find in
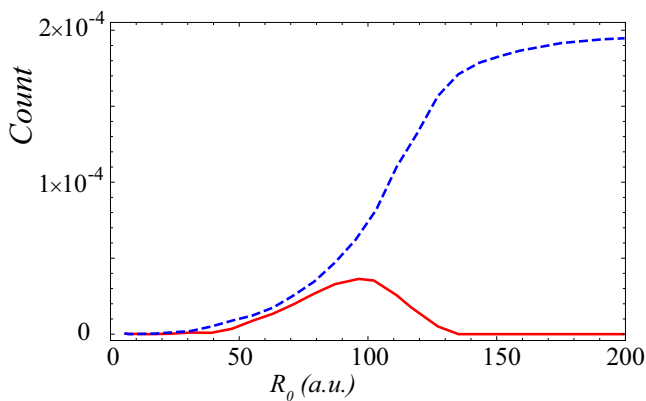

FIG. 11. Histogram of the initial conditions leading to formation (solid red line) and leading to dissociation (shaded blue line). The parameters of the laser are $F = 1.5 \times 10^{-3}$ a.u., $T_{ru} = T_{rd} = 15$ ps, and $T_p = 70$ ps. The energy of the trajectories is $E_0 = 3 \times 10^{-9}$ a.u.

this periodic orbit the same qualitative formation behavior observed in the full system. In other words, this information allows one to focus on the formation dynamics arising from the one-degree-of-freedom Hamiltonian associated with I_R, e.g., with a Hamiltonian model where the degree of freedom (θ, P_θ) is frozen.

IV. ONE-DEGREE-OF-FREEDOM MODEL

The codimension 2 manifolds defined by $\theta = k\pi/2$ ($k = 0,1,2$) and $P_\theta = 0$ are invariant under the dynamics. This allows us to define essentially two reduced Hamiltonian systems with $1+1/2$ degrees of freedom:

$$H_1(R,P_R,t) = \frac{P_R^2}{2\mu} + \varepsilon(R) - g(t)\frac{F^2}{4}\alpha_\parallel(R), \quad \text{for } \theta = 0,\pi,$$

(12)

and

$$H_2(R,P_R,t) = \frac{P_R^2}{2\mu} + \varepsilon(R) - g(t)\frac{F^2}{4}\alpha_\perp(R), \quad \text{for } \theta = \pi/2.$$

(13)

The model (12) describes the dynamics of the radial mode I_R and it is structurally stable, in the sense that if we move slightly away from this model by considering the full model in a range of values of θ and P_θ close to zero, the dynamics stays in the vicinity of the ones obtained with the model (12). On the contrary, the second model described by Hamiltonian (13) is structurally unstable since trajectories near $\theta = \pi/2$ and $P_\theta = 0$ tend to move away from these values in the full model. In this way, in what follows we focus on Hamiltonian (12). The corresponding equations of motion are

$$\dot{R} = \frac{P_R}{\mu},$$
$$\dot{P}_R = -\frac{d\varepsilon(R)}{dR} + g(t)\frac{F^2}{4}\frac{d\alpha_\parallel(R)}{dR}.$$

(14)

We consider an ensemble of initial conditions (R_0, P_R^0) with energy $E_0 = 3 \times 10^{-9}$ a.u. defined as

$$E_0 = \frac{P_{R_0}^2}{2\mu} + \varepsilon(R_0),$$

where the initial values of intermolecular distance R_0 are distributed in the interval $[R_{min}, R_{max}] = [6.2319, 100]$ a.u. according to the criterion described in Sec. III.

Using this ensemble of initial conditions, we compute the formation probability as a function of the electric field parameter F and the results are shown in Fig. 12. We notice that we find the same qualitative behavior as in the formation probability for the full Hamiltonian (1), notably the decrease of the probability for sufficiently large amplitudes.

After a ramp-up of 15 ps, the probability distribution of the energy is represented in Fig. 13 for the value $F = 1.5 \times 10^{-3}$ a.u. for which a significant formation probability is observed (see Fig. 12).

From the computation of the probability distribution of the energy after the ramp-up (red line in Fig. 13), we observe again a strong peak structure which indicates that, after the
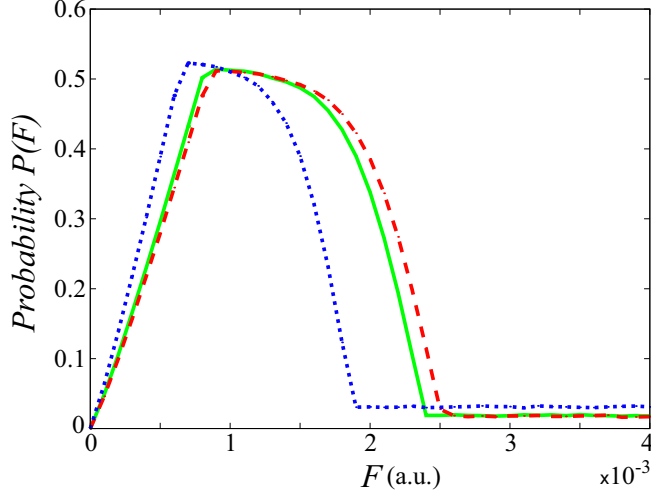
FIG. 12. Formation probability as a function of F for an initial energy $E_0 = 3 \times 10^{-9}$ a.u. computed using Hamiltonian (12). The parameters of the pulse are $T_{ru} = T_{rd} = 5$ ps and $T_p = 70$ ps (dashed red line), $T_{ru} = T_{rd} = 15$ ps and $T_p = 70$ ps (solid green line), and $T_{ru} = T_{rd} = 15$ ps and $T_p = 140$ ps (dotted blue line), respectively.

ramp-down, most of the trajectories have energies in a narrow region below the dissociation threshold $E_d = -F^2\alpha_\parallel(\infty)/4$. This is an expected behavior since the effect of the ramp-up is to decrease the initial energy E_0 of the trajectories and due to fact that E_0 is small, the energies of the trajectories after the ramp-up are below E_d.

Since the initial distances R_0 of our trajectories are in general large, we assume that, during the ramp-up, the intermolecular distances R do not change significantly since $\dot{R} = P_R/\mu$ is small. Under this assumption, an approximation of the momentum at the end of the ramp-up is obtained by considering that R is constant. Indeed, using the equations of motion (14), the variation of the radial momentum induced by
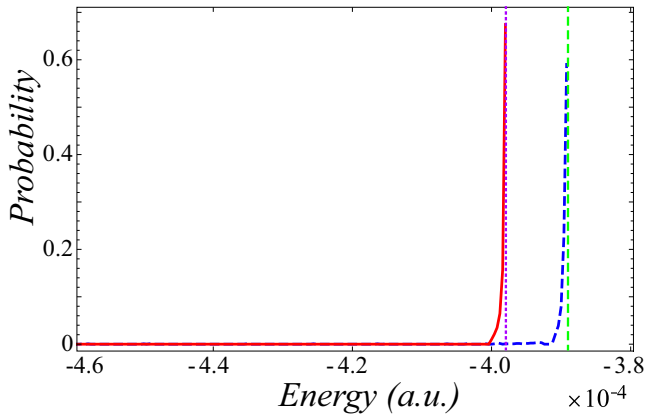

FIG. 13. Probability distributions of an ensemble of trajectories with an initial energy $E_0 = 3 \times 10^{-9}$ a.u. after a ramp-up of 15 ps obtained with formula (16) (solid red line) and with Hamiltonian (12) (dashed blue line). The amplitude of the laser field is $F = 1.5 \times 10^{-3}$ a.u. The dashed green vertical line indicates the dissociation energy $E_d = -F^2\alpha_\parallel(\infty)/4$ while the dotted purple vertical line denotes the energy $E_d = -F^2\alpha_\parallel(R_{max})/4$.
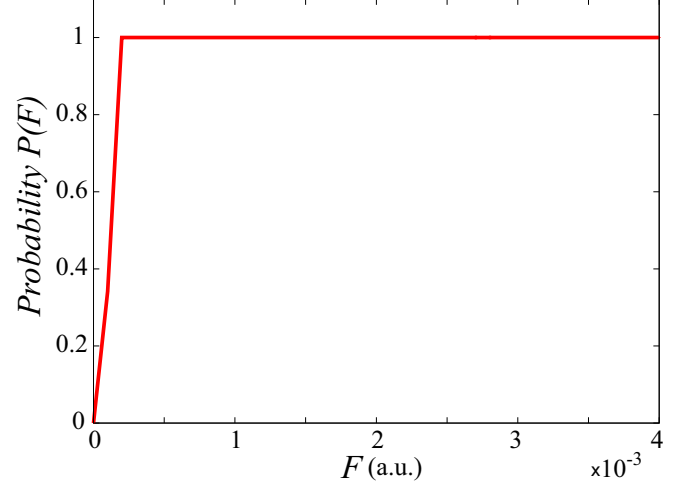

FIG. 14. Formation probability for Hamiltonian (12) as a function of F for an initial energy $E_0 = 3 \times 10^{-9}$ a.u. The parameters of the pulse are $T_{ru} = 15$ ps, $T_p = 70$ ps, and no ramp-down.

the ramp-up of the field is approximately given by

$$\Delta P_R(T_{ru}) \approx \frac{F^2}{8} T_{ru} \frac{d\alpha_\parallel(R_0)}{dR}, \tag{15}$$

where the term of order F^4 is neglected and we assume that $d\varepsilon(R_0)/dR \approx 0$. Since $d\alpha_\parallel(R_0)/dR$ is negative (see Fig. 1) for most of the values of R_0, we conclude that, in general, the momentum decreases as a result of the ramp-up. In order to have an approximate value of the energy at the end of the ramp-up of the laser field for large values of R_0, we insert Eq. (15) into Hamiltonian (12). After neglecting the term of order F^4, we get

$$E_{ru} \approx E_0 - \frac{F^2}{4}\alpha_\parallel(R_0) + \frac{F^2 T_{ru}}{8\mu} P_R^0 \alpha'_\parallel(R_0). \tag{16}$$

In order to check the validity of the above equation, we compute the probability distribution of the energy for our set of initial conditions by using Eq. (16). The result (blue line in Fig. 13) is rather accurate since the probability distribution obtained from Eq. (16) is closely peaked below the value $E = -F^2\alpha_\parallel(R_{max})/4$.

During the plateau, the Hamiltonian (12) has one degree of freedom and the energy of the system is conserved. Since for relevant values of F, all the energies are below the dissociation threshold $E_d = -F^2\alpha_\parallel(\infty)/4$, all the trajectories remain bounded during the plateau. This is confirmed in Fig. 14 where the formation probability, computed from an energy criterion $E < E_d = -F^2\alpha_\parallel(\infty)/4$, is represented as a function of F.

It means that at all times, all the dimers remain bounded in the presence of the laser field for $F \gtrsim 2 \times 10^{-4}$ a.u., whether a distance or an energy criterion is used. During the plateau, all the bounded trajectories are periodic and their periods are given by

$$T(E,F) = \sqrt{2\mu} \int_{R_a(E,F)}^{R_b(E,F)} \frac{dR}{\sqrt{E - \varepsilon(R) + \frac{F^2}{4}\alpha_\parallel(R)}}, \tag{17}$$
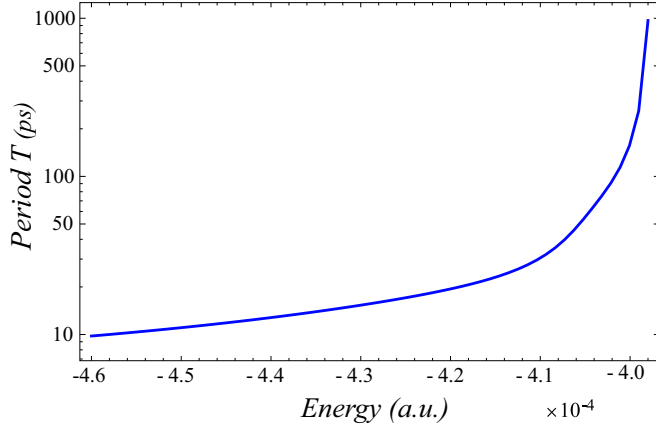
FIG. 15. Periods of our ensemble of trajectories for $F = 1.5 \times 10^{-3}$ a.u. using Eq. (17). Note the logarithmic scale in the vertical axis.

where $R_a < R_b$ are the two turning points given by the solutions of

$$\varepsilon(R) - \frac{F^2}{4}\alpha_\parallel(R) = E < E_d.$$

Since the ramp-up promotes most of the trajectories very close but below the threshold energy values E_d, we have computed the periods of our ensemble of trajectories for $F = 1.5 \times 10^{-3}$ a.u. The results are shown in Fig. 15. As expected, the motion is very slow in comparison with the duration of the pulse and it mirrors the observation made in the first recurrence time map of Fig. 8.

As we have observed, after the ramp-up and for relevant values of F, most of the trajectories remain bounded during the plateau. However, not all these bounded dressed states, i.e., the bounded states in the presence of the laser field, remain bounded after the ramp-down. Even for this one-dimensional model it is cumbersome to untangle the effects of the various parts of the pulse and to provide insights into the role of the parameters of the pulse. In order to unravel the dynamics, we consider the long-range dynamics of the one-degree-of-freedom Hamiltonian model (12).

V. SIMPLIFIED POTENTIAL

In order to investigate the long-range behavior of Hamiltonian (12), we assume that, for R large, the expressions of the functions defining the potential are [see Eqs. (5) and (8)],

$$\varepsilon(R) \approx -\frac{b_6}{R^6}, \tag{18}$$

$$\alpha_\parallel(R) \approx \alpha_{\mathrm{RbCs}} + \frac{d_2}{R^2} + \frac{d_3}{R^3}, \tag{19}$$

and the simplified long-range Hamiltonian becomes

$$H_s = \frac{P_R^2}{2\mu} - \frac{b_6}{R^6} - g(t)\frac{F^2}{4}\left(\alpha_{\mathrm{RbCs}} + \frac{d_2}{R^2} + \frac{d_3}{R^3}\right). \tag{20}$$

The formation probability computed using Hamiltonian (20) as a function of F is shown in Fig. 16. This formation probability (green line in Fig. 16) is in very close
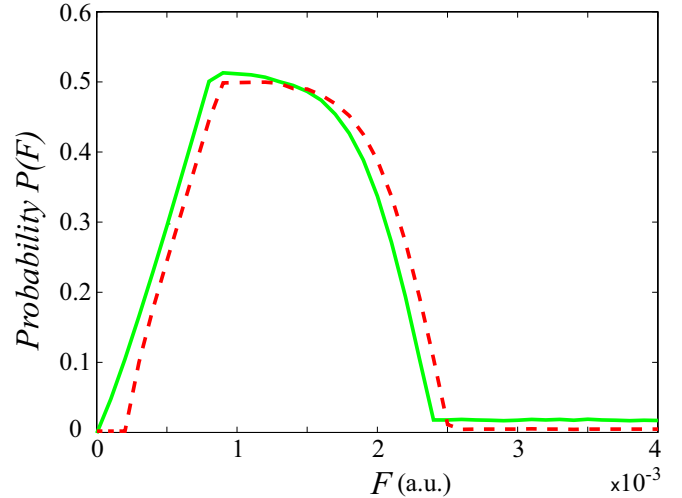

FIG. 16. Formation probability as a function of F for an initial energy $E_0 = 3 \times 10^{-9}$ a.u. obtained from the long-range Hamiltonian (20) (dashed red line) and the full Hamiltonian (12) (solid green line). The parameters of the pulse are $T_{\mathrm{ru}} = T_{\mathrm{rd}} = 15\,\mathrm{ps}$ and $T_{\mathrm{p}} = 70\,\mathrm{ps}$.

agreement with the formation probability obtained with the full Hamiltonian (12) (red line in Fig. 16), which validates the approximate expressions (18) and (19) of the potentials.

In order to get some insight into this probability curve, we compute the momentum transfer during the laser pulse as

$$\Delta P_R = \frac{F^2}{4}\int_0^{T_{\mathrm{ru}}+T_{\mathrm{p}}+T_{\mathrm{rd}}} g(t)\,\frac{d\alpha_\parallel(R)}{dR}\,dt. \tag{21}$$

where we again assume that $d\varepsilon(R)/dR \approx 0$. Initially, the momentum is given by

$$P_R^0 = \pm\sqrt{2\mu[E_0 - \varepsilon(R_0)]}.$$

For example, for $R = 50$ a.u. the initial value of the momentum is $P_R^0 \approx 0.3$ a.u. and the radial velocity is $\dot{R}(0) \approx 3 \times 10^{-6}$ a.u. As a consequence, $\dot{R}(0)$ is small and, therefore, it is reasonable (at least at the leading order) to assume that R is approximately constant. Using this assumption, the shape of the laser pulse given by Eq. (4) and the expression (21), the momentum transfer induced by the pulse is given by

$$\Delta P_R = \frac{F^2(T_{\mathrm{ru}} + 2T_{\mathrm{p}} + T_{\mathrm{rd}})}{8}\frac{d\alpha_\parallel(R)}{dR}. \tag{22}$$

We notice that $\Delta P_R < 0$ since $d\alpha_\parallel(R)/dR$ is always negative. This small momentum transfer, which is of the same order as P_R^0, is responsible for the formation, even though this momentum transfer does not have significantly impact on the variation of the interatomic distance on the short time scale of the laser pulse. Furthermore, the dependence of the momentum transfer on the parameters of the laser pulse is rather simple since the only involved parameter is $T_{\mathrm{ru}} + 2T_{\mathrm{p}} + T_{\mathrm{rd}}$. In fact, the dependence as a function of F and the parameters of the laser pulse can be encapsulated in a single effective parameter

$$f = \frac{F}{2\sqrt{2}}\sqrt{T_{\mathrm{ru}} + 2T_{\mathrm{p}} + T_{\mathrm{rd}}},$$
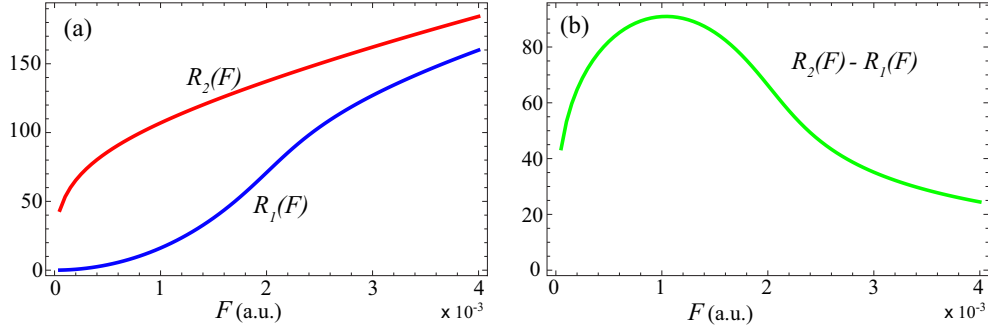
FIG. 17. (a) Evolution as a function of F of the roots R_1 and R_2 of $E(R)$ given by Eq. (24). (b) Evolution of $R_2 - R_1$ as a function of F. The parameters of the pulse are $T_{ru} = 15\,\text{ps}$, $T_p = 70\,\text{ps}$, and $T_{rd} = 15\,\text{ps}$.

so that for a fixed value of f, the formation probability no longer depends on the parameters of the laser pulse. Using the momentum transfer (22), the energy at the end of the laser pulse is

$$E_f = E_0 + \frac{P_R^0 \Delta P_R}{\mu} + \frac{(\Delta P_R)^2}{2\mu}. \tag{23}$$

According to Eq. (23), there is formation if $E_f < 0$. Since ΔP_R is negative, the final energy E_f can only be negative (i.e., resulting in a formation) if P_R^0 is positive. This is a necessary but not a sufficient condition. If F is too small, the final energy remains positive (and close to E_0) since the negative term is insufficient to compensate for E_0, so there is no possibility for formation. If F is too large, the dominant term in Eq. (23) is $(\Delta P_R)^2/(2\mu)$ which is positive, therefore resulting in a positive final energy, and there is no formation. This qualitatively gives the explanation for the increase of the formation probability for small F and the decrease for large F.

In order to be more quantitative, we consider Eq. (23) for $P_R^0 > 0$ as a general function $E(R)$ in the variable R and which depends on the parameter f,

$$E(R) = E_0 - f^2 \sqrt{\frac{2}{\mu}\left(E_0 + \frac{b_6}{R^6}\right)\left(\frac{2d_2}{R^3} + \frac{3d_3}{R^4}\right)} + \frac{f^4}{2\mu}\left(\frac{2d_2}{R^3} + \frac{3d_3}{R^4}\right)^2. \tag{24}$$

When $R \to \infty$, $E(R)$ tends to E_0 and when $R \to 0$, $E(R)$ tends to $+\infty$. The function $E(R)$ has two roots $R_1(f)$ and $R_2(f)$ such that $R_1(f) < R_2(f)$. Because the function $E(R)$ is negative between these two roots, if the interatomic distance is in the region where $E(R)$ is negative, e.g., between the roots $R_1(f)$ and $R_2(f)$, then there is formation.

Figure 17 shows the evolutions of $R_{1,2}(F)$ and $R_2(F) - R_1(F)$ as a function of F. We notice that the distance $R_2 - R_1$ first increases with F until $F \approx 10^{-3}$ a.u. and then decreases. This behavior mirrors the increase and decrease of the formation probability as a function of F.

In the appendix, we derive some approximate expansions for the zeros of $E(R)$ and deduce two expansions for $R_2 - R_1$, one for small values of F and one for larger values of F. In a nutshell, these expansions lead to the following behaviors: For small F, the formation probability increases as $F^{2/7}$, and for

large F, it roughly decreases with F as $1/F$. More specifically, we have

$$R_2(f) - R_1(f) \approx \left(\frac{3d_3\sqrt{2b_6}}{E_0\sqrt{\mu}}\right)^{1/7} f^{2/7} \qquad \text{for} \quad f \ll 1, \tag{25}$$

$$R_2(f) - R_1(f) \approx \frac{b_6^{1/2}(2\mu)^{1/4}}{2\sqrt{3d_3}E_0^{1/4}f}$$
$$- \frac{b_6^{1/2}d_2(2\mu)^{1/8}}{4E_0^{3/8}(3d_3)^{5/4}f^{1/2}} \qquad \text{for} \quad f \gg 1. \tag{26}$$

Naturally, for an ensemble of values of R_0 between $R_{\min}$ and $R_{\max}$, we consider the overlap between the intervals $[R_{\min}, R_{\max}]$ and $[R_1(f), R_2(f)]$, so that an approximation of the formation probability is given by

$$P(f) = \frac{\min[R_{\max}, R_2(f)] - \max[R_{\min}, R_1(f)]}{2(R_{\max} - R_{\min})}, \tag{27}$$

if $R_1(f) \leqslant R_{\max}$ and $R_2(f) \geqslant R_{\min}$; otherwise the probability is zero since there is no overlap between the available values of R_0 and the values of R leading to a negative energy. The coefficient $1/2$ in the probability expression (27) comes from the fact that for a given R, there are two possible initial values for P_R^0, one positive (and possibly leading to formation) and another one negative (not leading to formation) with the same energy E_0. The blue curve on Fig. 18 is the formation probability obtained using the numerical computation of the roots of $E(R)$ and using Eq. (27). The agreement with the numerical integration of the trajectories for the simplified Hamiltonian (20) as well as with the full one-dimensional Hamiltonian (12) is very good, validating the assumptions on the dynamics of the trajectories leading to the approximation (27) for the formation probability.

The main reason for the rather good quantitative agreement is that, in the interval $[R_{\min}, R_{\max}]$, a large portion of the initial values of R are large and the approximations performed to derive Eq. (27) are valid.

Three parameters emerge as most influential in the formation probability. All of them are related to the long-range behavior of the dimer. One is related to the dimer potential (behavior as $1/R^6$) and two are linked with the parallel
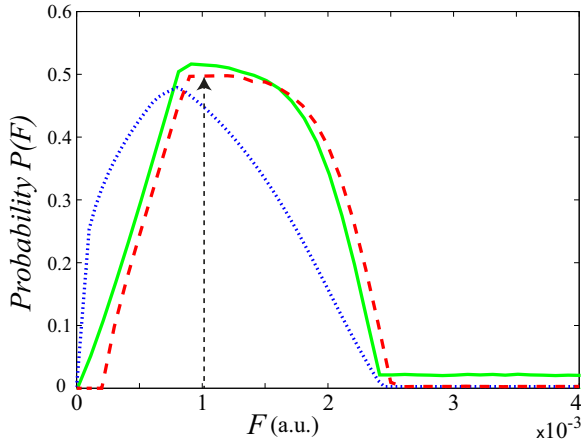
FIG. 18. Formation probability given by Eq. (27) as a function of F (dotted blue line). For completeness, the formation probability as a function of F obtained from the long-range Hamiltonian (20) (dashed red line) and from the full Hamiltonian (12) (solid green line) are also shown. The black vertical dashed arrow is located at the value $F \approx 0.00107$ a.u. given by Eq. (28). For this value of F, it is expected to find the maximum of the formation probability. The parameters of the pulse are $T_{ru} = 15$ ps, $T_p = 70$ ps, and $T_{rd} = 15$ ps. The initial energy of the trajectories is $E_0 = 3 \times 10^{-9}$ a.u.

polarizability (behaviors as $1/R^2$ and $1/R^3$). It should be noticed that the term in $1/R^6$ in the potential $\varepsilon(R)$ is absolutely essential to ensure the existence of the two roots of $E(R)$.

In the appendix we also provide an approximate expression for the value of the electric field amplitude where a maximum of formation is expected and it is given by

$$F \approx \frac{2\sqrt{2}}{\sqrt{T_{ru} + 2T_p + T_{rd}}}. \tag{28}$$

For a laser pulse with parameters $T_{ru} = 15$ ps, $T_p = 70$ ps, and $T_{rd} = 15$ ps, according to Eq. (28), the maximum of formation is expected at $F \approx 0.00107$ a.u. As we can observe in Fig. 18, this value lies in the neighborhood of the values of F where the computed formation probability is maximum.

In addition, we have shown in the appendix the rather small dependence of the formation probability with respect to the initial energy of the system (or equivalently, to its temperature).

VI. CONCLUSION

The classical study carried out in this paper shows the feasibility of using an intense linearly polarized laser field to drive the association of Rb and Cs cold atoms to create a dimer in its ground state. Interestingly, from our numerical calculations of the evolution of the formation probability as a function of the electric field strength of the laser, we find that the formation probability first increases and then decreases with increasing laser field intensity. In order to explain this surprising behavior of the formation probability, we use nonlinear dynamics and we show that the main element responsible for the formation of RbCs is a rather small change in the radial momentum P_R induced by the laser pulse through its interaction with the molecular polarizability. This change of radial momentum is so small that it is not sufficient to

induce changes in the positions of the atoms on the short time scale of the laser pulse. However, it is sufficient to allow the formation of RbCs dimers. Furthermore, the behavior of the formation probability reflects the long-range behavior of the dimer. The deep impact of the long-range behavior of the molecule in the formation mechanism allows us to reduce the dynamics to a one-dimensional radial Hamiltonian where only the long-range terms of the potential are taken into account. With this simplified Hamiltonian, we explained why initially positive momentum leads to higher formation and why an initially too short or too large interatomic distance [i.e., shorter than $R_1(f)$ or larger than $R_2(f)$] does not lead to formation. Moreover, from these observations and using that one-dimensional Hamiltonian, we have derived the approximate expression (27) for the formation probability which highlights the role of the relevant parameters of the laser pulse and of the interaction potential which lead to the shaping of the formation probability. In particular, such an expression might be helpful to control the formation probability by adjusting the parameters of the laser field. Finally, a quantum extension of our classical approach to the driven formation of cold dimers is of immediate interest in order to predict the quantum association rate which could be compared to experiments. Work along this line is now in progress.

APPENDIX: APPROXIMATE EXPRESSIONS FOR THE ZEROS OF THE FUNCTION $E(R)$

In order to obtain the asymptotic behaviors of the zeros of Eq. (24) and hence of the formation probability, we rewrite $E(R)$ as

$$E(R) = \frac{1}{2}\left[X - \sqrt{2\left(E_0 + \frac{b_6}{R^6}\right)} \right]^2 - \frac{b_6}{R^6},$$

where

$$X = \frac{f^2}{\sqrt{\mu}}\left(\frac{2d_2}{R^3} + \frac{3d_3}{R^4} \right).$$

The zeros of $E(R)$ satisfy

$$X_{\pm} = \sqrt{2\left(E_0 + \frac{b_6}{R^6}\right)} \pm \sqrt{\frac{2b_6}{R^6}}. \tag{A1}$$

The above equation corresponds to two implicit equations for R_1 and R_2. The branch with X_+ corresponds to R_1 and the one with X_- to R_2. When f tends to zero, the two solutions R_1 and R_2 converge to zero. Using an expansion of Eq. (A1)

around $R = 0$, we obtain the asymptotic behaviors

$$R_1(f) \approx \frac{3d_3}{2\sqrt{2\mu b_6}} f^2, \tag{A2}$$

$$R_2(f) \approx \left(\frac{3d_3\sqrt{2b_6}}{E_0\sqrt{\mu}} \right)^{1/7} f^{2/7}. \tag{A3}$$

As a consequence, if $[R_1, R_2] \subset [R_{\min} R_{\max}]$, the formation probability increases as $f^{2/7}$. It is worth noticing that there is a very slight dependence on the initial energy (i.e., on the temperature T of the gas) since the approximate formation probability behaves as $T^{-1/7}$.

For large values of f, the two roots $R_1(f)$ and $R_2(f)$ tend to infinity with the same asymptotic behavior given by $R_0(f)$ solution of

$$\frac{f^2}{\sqrt{\mu}} \left(\frac{2d_2}{R^3} + \frac{3d_3}{R^4} \right) = \sqrt{2E_0}.$$

An explicit solution of $R_0(f)$ can be obtained since it is a solution of a quartic polynomial. However, this expression is not very helpful. An expansion of the solution is given by

$$R_0(f) = 3^{1/4} d_3^{1/4} \frac{\sqrt{f}}{(2\mu E_0)^{1/8}} + \frac{d_2}{2\sqrt{3d_3}} \frac{f}{(2\mu E_0)^{1/4}} + O(f^{5/4}).$$

The two roots $R_1(f)$ and $R_2(f)$ tend to $R_0(f)$ as f increases, and the distance between the two roots decreases

as

$$R_2(f) - R_1(f) \approx \frac{b_6^{1/2}(2\mu)^{1/4}}{2\sqrt{3d_3}E_0^{1/4}f} - \frac{b_6^{1/2}d_2(2\mu)^{1/8}}{4E_0^{3/8}(3d_3)^{5/4}f^{1/2}}. \tag{A4}$$

Given the values of the coefficients, we expect the formation probability to decrease as f increases. The leading behavior is proportional to f^{-1} but the second term is of the same order, so it needs to be taken into account for a more quantitative agreement (see Fig. 17). We notice the strong dependence of the formation probability with one of the parameters of the potential $\varepsilon(R)$, namely b_6, as well as the two main parameters of the parallel polarizability, namely d_2 and d_3. In addition, there is a slight dependence of the initial energy (or equivalently the temperature): It increases as the temperature decreases. The leading behavior is $T^{-1/4}$. Using Eqs. (A3) and (A4), we obtain an approximate value of F for the expected maximum of $R_2 - R_1$:

$$f_* = \frac{b_6^{1/3}\mu^{1/4}}{2^{23/36}(3d_3)^{1/2}E_0^{1/12}}.$$

In particular we notice the very small dependence of this value with the initial energy, i.e., the temperature of the gas. As a rule of thumb, $f_* \approx 1$, so the expected maximum for the formation probability is approximately obtained for

$$F_* \approx \frac{2\sqrt{2}}{\sqrt{T_{\rm ru} + 2T_{\rm p} + T_{\rm rd}}}.$$

[1] M. H. Anderson, J. R. Ensher, M. R. Matthews, C. E. Wieman, and E. A. Cornell, Science **269**, 198 (1995).

[2] K. B. Davis, M.-O. Mewes, M. R. Andrews, N. J. van Druten, D. S. Durfee, D. M. Kurn, and W. Ketterle, Phys. Rev. Lett. **75**, 3969 (1995).

[3] C. C. Bradley, C. A. Sackett, and R. G. Hulet, Phys. Rev. Lett. **78**, 985 (1997).

[4] B. DeMarco and D. S. Jin, Science **285**, 1703 (1999).

[5] K. M. O'Hara, S. R. Granade, M. E. Gehm, T. A. Savard, S. Bali, C. Freed, and J. E. Thomas, Phys. Rev. Lett. **82**, 4204 (1999).

[6] A. G. Truscott, K. E. Strecker, W. I. McAlexander, G. B. Partridge, and R. G. Hulet, Science **291**, 2570 (2001).

[7] K. M. Jones, E. Tiesinga, P. D. Lett, and P. S. Julienne, Rev. Mod. Phys. **78**, 483 (2006).

[8] K.-K. Ni, S. Ospelkaus, D. J. Nesbitt, J. Ye, and D. S. Jin, Phys. Chem. Chem. Phys. **11**, 9626 (2009).

[9] T. Takekoshi, L. Reichsöllner, A. Schindewolf, J. M. Hutson, C. R. Le Sueur, O. Dulieu, F. Ferlaino, R. Grimm, and H.-C. Nägerl, Phys. Rev. Lett. **113**, 205301 (2014).

[10] A. J. Kerman, J. M. Sage, S. Sainis, T. Bergeman, and D. De Mille, Phys. Rev. Lett. **92**, 033004 (2004).

[11] J. G. Danzl, E. Haller, M. Gustavsson, M. J. Mark, R. Hart, N. Bouloufa, O. Dulieu, H. Ritsch, and H.-C. Nägerl, Science **321**, 1062 (2008).

[12] J. G. Danzl, M. J. Mark, E. Haller, M. Gustavsson, R. Hart, J. Aldegunde, J. M. Hutson, and H.-C. Nägerl, Nat. Phys. **6**, 265 (2010).

[13] S. D. Kraft, P. Staanum, J. Lange, L. Vogel, R. Wester, and M. Weidemüller, J. Phys. B **39**, S993 (2006).

[14] K.-K. Ni, S. Ospelkaus, M. H. G. de Miranda, A. Pe'er, B. Neyenhuis, J. J. Zirbel, S. Kotochigova, P. S. Julienne, D. S. Jin, and J. Ye, Science **322**, 231 (2008).

[15] M. Debatin, T. Takekoshi, R. Rameshan, L. Reichsöllner, F. Ferlaino, R. Grimm, R. Vexiau, N. Bouloufa, O. Dulieu, and H.-C. Nägerl, Phys. Chem. Chem. Phys. **13**, 18926 (2011).

[16] T. Takekoshi, M. Debatin, R. Rameshan, F. Ferlaino, R. Grimm, H.-C. Nägerl, C. R. Le Sueur, J. M. Hutson, P. S. Julienne, S. Kotochigova, and E. Tiemann, Phys. Rev. A **85**, 032506 (2012).

[17] M. P. Köppinger, D. J. McCarron, D. L. Jenkin, P. K. Molony, H.-W. Cho, S. L. Cornish, C. R. Le Sueur, C. L. Blackley, and J. M. Hutson, Phys. Rev. A **89**, 033604 (2014).

[18] C. Haimberger, J. Kleinert, O. Dulieu, and N. P. Bigelow, J. Phys. B **39**, S957 (2006).

[19] E. Juarros, P. Pellegrini, K. Kirby, and R. Côté, Phys. Rev. A **73**, 041403(R) (2006).

[20] P. S. Zuchowski and J. M. Hutson, Phys. Rev. A **81**, 060703(R) (2010).

[21] L. D. Carr, D. DeMille, R. V. Krems, and J. Ye, New J. Phys. **11**, 055049 (2009).

[22] A. Friedrich and D. Wintgen, Phys. Rep. **183**, 37 (1989).

[23] J. Main, M. Schwacke, and G. Wunner, Phys. Rev. A **57**, 1149 (1998).

[24] J. Main and G. Wunner, Phys. Rev. Lett. **82**, 3038 (1999).

[25] C. A. Arango, W. W. Kennerly, and G. S. Ezra, Chem. Phys. Lett. **392**, 486 (2004).

[26] M. Iñarrea, V. Lanchares, J. F. Palacián, A. I. Pascual, J. P. Salas, and P. Yanguas, Phys. Rev. A **76**, 052903 (2007).

[27] J. P. Salas, Eur. Phys. J. D. **41**, 95 (2007).

[28] C. A. Arango and G. S. Ezra, Int. J. Bifurc. Chaos **18**, 1127 (2008).

[29] S. Huang, C. Chandre, and T. Uzer, J. Chem. Phys. **128**, 174105 (2008).

[30] M. Iñarrea, J. P. Salas, R. González-Férez, and P. Schmelcher, Phys. Lett. A **374**, 457 (2010).

[31] A. Junginger, J. Main, and G. Wunner, Phys. Rev. A **86**, 012713 (2012).

[32] A. Kamor, F. Mauger, C. Chandre, and T. Uzer, Phys. Rev. Lett. **110**, 253002 (2013).

[33] M. Gutzwiller, *Chaos in Classical and Quantum Mechanics* (Springer-Verlag, New York, 1990).

[34] A. D. Peters, C. Jaffe, and J. B. Delos, Phys. Rev. Lett. **73**, 2825 (1994).

[35] K. A. Mitchell, J. P. Handley, B. Tighe, A. Flower, and J. B. Delos, Phys. Rev. Lett. **92**, 073001 (2004).

[36] R. Blümel and W. P. Reinhardt, *Chaos in Atomic Physics*, Cambridge Monographs on Atomic, Molecular, and Chemical Physics (Cambridge Univerity Press, Cambridge, 1997).

[37] M. J. Norman, C. Chandre, T. Uzer, and P. Wang, Phys. Rev. A **91**, 023406 (2015).

[38] R. Grobe and C. K. Law, Phys. Rev. A **44**, R4114 (1991).

[39] T. Seideman, J. Chem. Phys. **107**, 10420 (1997).

[40] J. Deiglmayr, M. Aymar, R. Wester, M. Weidemüller, and O. Dulieu, J. Chem. Phys. **129**, 064309 (2008).

[41] C. M. Dion, A. Keller, O. Atabek, and A. D. Bandrauk, Phys. Rev. A **59**, 1382 (1999).

[42] S. Trippel, T. Mullins, N. L. M. Müller, J. S. Kienitz, J. J. Omiste, H. Stapelfeldt, R. González-Férez, and J. Küpper, Phys. Rev. A **89**, 051401 (2014).

[43] A. R. Allouche, M. Korek, K. Fakherddin, A. Chaalan, M. Dagher, F. Taher, and M. Aubert-Frécon, J. Phys. B: At. Mol. Opt. Phys. **33**, 2307 (2000).

[44] M. Marinescu and H. R. Sadeghpour, Phys. Rev. A **59**, 390 (1999).

[45] L. Silberstein, Philos. Mag. **33**, 521 (1917).

[46] L. Jensen, P. O. Astrand, A. Osted, J. Kongsted, and K. V. Mikkelsen, J. Chem. Phys. **116**, 4001 (2002).

[47] R. González-Férez and P. Schmelcher, Phys. Rev. A **69**, 023402 (2004).

[48] R. González-Férez and P. Schmelcher, Phys. Rev. A **71**, 033416 (2005).

[49] J. M. Rost, J. C. Griffin, B. Friedrich, and D. R. Herschbach, Phys. Rev. Lett. **68**, 1299 (1992).

[50] S. M. Purcell and P. F. Barker, Phys. Rev. A **82**, 033433 (2010).

[51] A. Amelink and P. van der Straten, Phys. Scr. **68**, C82 (2003).